

# Antiferromagnetic coupling of the single-molecule magnet $\text{Mn}_{12}$ to a ferromagnetic substrate

Kyungwha Park

*Department of Physics, Virginia Tech, Blacksburg, Virginia, 24061*

(Dated: May 31, 2021)

## Abstract

We investigate magnetic coupling between a monolayer of prototype single-molecule magnets  $\text{Mn}_{12}$  and a ferromagnetic Ni(111) substrate through S, using density-functional theory (DFT) and a DFT+ $U$  method. Our DFT and DFT+ $U$  calculations show that the  $\text{Mn}_{12}$  molecules favor antiferromagnetic coupling to the Ni substrate, and that they possess magnetic moments deviated from the magnetic moments of isolated  $\text{Mn}_{12}$  molecules. We find that the magnetic easy axis of the  $\text{Mn}_{12}$  on Ni (whole system) is dictated by that of the Ni substrate. The antiferromagnetic coupling is, dominantly, caused by superexchange interactions between the magnetic moments of the Mn and the Ni substrate via the S, C, and O anions. Our findings can be observed from x-ray magnetic circular dichroism or scanning tunneling microscopy.

PACS numbers: 75.30.Et, 75.50.Xx, 75.70.-i, 71.15.Mb

## I. INTRODUCTION

Recently, tailoring static and dynamic magnetic properties of individual atoms and molecules by local environmental factors or local probes has drawn a lot of attention. This aligns with an effort to develop efficient devices for magnetic storage, spin transfer, molecular spintronics, or quantum computation, based on nanometer-sized magnetic atoms or molecules. One promising candidate for such devices is a group of single-molecule magnets (SMMs) consisting of several transition metal ions interacting through ligands. An individual SMM has a large magnetic moment and a high magnetic anisotropy barrier caused by spin-orbit coupling (SOC) and Jahn-Teller distortions<sup>1,2</sup>. In order to build devices including magnetic molecules, stable monolayers of magnetic molecules must be formed on various substrates, and mechanisms of interactions between molecules and substrates should be understood. A great progress has been made for deposition of various SMMs, such as prototype SMM  $\text{Mn}_{12}$ <sup>3-8</sup>,  $\text{Mn}_6$ <sup>9</sup>,  $\text{Fe}_4$ <sup>10</sup>,  $\text{Cr}_7\text{Ni}$ <sup>11</sup>, and  $\text{TbPc}_2$ <sup>12</sup>, on metallic, semiconducting, or superconducting substrates<sup>13</sup>. Electronic and magnetic properties of SMMs on substrates were characterized using x-ray absorption and photoemission spectroscopy<sup>4,6,9-11</sup>, scanning tunneling microscopy (STM)<sup>3,7,12</sup>,  $\beta$ -detected nuclear magnetic resonance<sup>5</sup>, and x-ray magnetic circular dichroism (XMCD)<sup>8,10</sup>. On the theoretical front, the electronic structure and magnetic properties of a SMM  $\text{Mn}_{12}$  monolayer adsorbed on Au were studied using density-functional theory (DFT)<sup>14</sup>. The theoretical calculations<sup>14</sup> revealed that the  $\text{Mn}_{12}$  molecules are weakly coupled to the Au substrate, and that charge and spin transfer occurs from the Au substrate to the  $\text{Mn}_{12}$ , mainly, through linker molecules.

Despite the great advances made in recent years, studies of SMMs adsorbed on substrates are currently limited to non-magnetic substrates. An understanding of magnetic coupling between SMMs and ferromagnetic (FM) substrates is, however, of a great importance for device applications and for investigation of properties of SMMs. For instance, the magnetic coupling can be used to control the reversals of the magnetic moments of SMMs or of the magnetization of FM substrates, depending on the coercive field strength of the SMMs relative to that of the FM substrates, similarly to exchange-bias systems<sup>15</sup>. Additionally, the magnetic coupling can influence electron transport properties through SMMs bridged between FM electrodes.

In this work, we examine magnetic coupling between a monolayer of SMMs  $\text{Mn}_{12}$  and

a FM Ni(111) substrate, using DFT and a DFT+U method<sup>16,17</sup>. We consider a structure where SMMs Mn<sub>12</sub> are adsorbed on a Ni substrate via two S atoms. Our DFT and DFT+U calculations show that the Mn<sub>12</sub> molecules prefer antiferromagnetic (AFM) coupling to the Ni substrate, and that their magnetic moments differ from the magnetic moments of isolated Mn<sub>12</sub> molecules. We find that the magnetic easy axis of the adsorbed Mn<sub>12</sub> is determined by the magnetic easy axis of the Ni substrate which depends on a thickness of the substrate. We also clarify mechanisms of the magnetic coupling by taking into account direct exchange coupling such as hybridization and an indirect exchange coupling mechanism such as superexchange interactions<sup>18</sup>. We find that superexchange interactions prevail over direct exchange in the magnetic coupling. Our results can be observed in experiments such as XMCD or STM.

The outline of this paper is as follows. We introduce our computational methods in Sec.II. We systematically construct a Mn<sub>12</sub> monolayer adsorbed on a Ni substrate via S, as well as present properties of an isolated Mn<sub>12</sub> and a bare Ni slab in Sec.III. We discuss the sign, magnitude, and mechanisms of the magnetic coupling between the Mn<sub>12</sub> and the Ni substrate, and the electronic and magnetic properties of the system of interest in Sec.IV. Finally, we make our conclusion in Sec.V.

## II. COMPUTATIONAL METHODS

We use two DFT codes, SIESTA<sup>19</sup> and VASP<sup>20</sup>, to compute the electronic structure and magnetic properties of a Mn<sub>12</sub> monolayer on Ni(111). SIESTA uses localized numerical atomic orbitals as basis sets, while VASP uses plane waves. In both SIESTA and VASP calculations, we use the Perdew-Burke-Ernzerhopf (PBE) generalized-gradient approximation (GGA)<sup>21</sup> for exchange-correlation potential. We do not include SOC in our calculations unless specified otherwise. First, we discuss set-ups and parameters for SIESTA calculations. We use Troullier-Martins pseudopotentials<sup>22,23</sup> with scalar relativistic terms and core corrections for all the elements except H. We construct corresponding basis sets as discussed in Refs.[24,25]. For Mn, we include 3*p* orbitals in valence states. For Ni, we use a default basis set of DZP. We use a mesh cutoff of 400 Ry. We carry out self-consistent calculations until a density matrix converges to within  $3 \times 10^{-5}$ . Second, we discuss set-ups and parameters for VASP calculations. We use projector-augmented-wave (PAW) pseudopotentials<sup>26</sup> for all the ele-

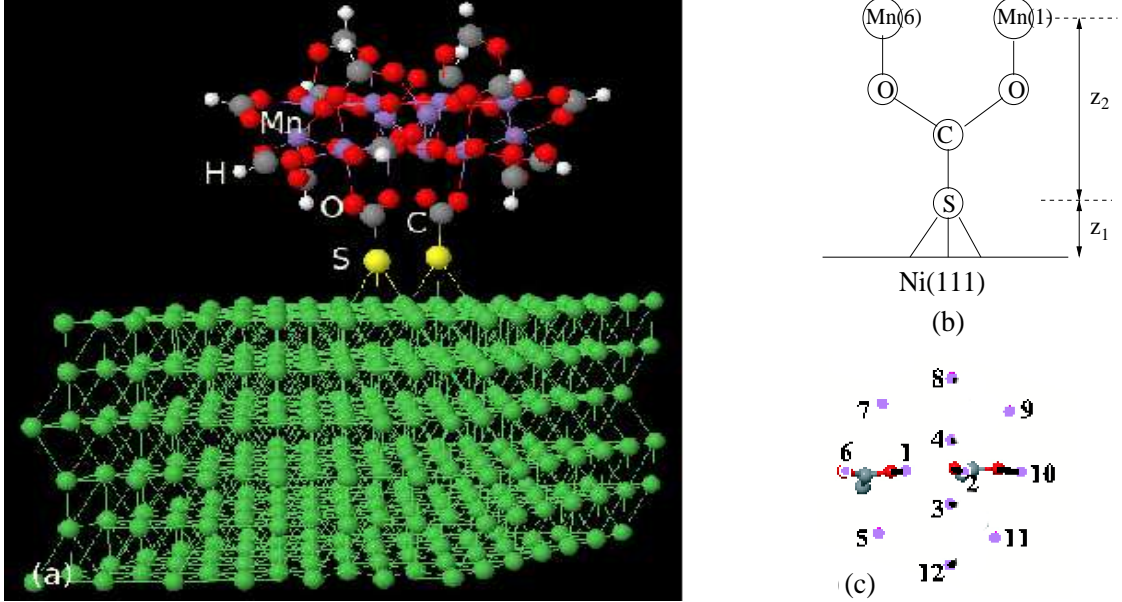


FIG. 1: (Color online) (a) Side view of the whole structure: a SMM Mn<sub>12</sub> adsorbed on a FM Ni(111) slab of six atomic layers, via two S atoms. (b) Part of the interface region. The vertical distances,  $z_1$  and  $z_2$ , are listed in Table I. (c) Top view (in the  $xy$  plane) showing the twelve Mn ions labeled, the O bonded to the Mn(1), Mn(2), Mn(6), and Mn(10) sites, and the C bonded to the O and S. Modified from Ref.[29].

ments. For Mn, we consider  $3p$  orbitals as a semicore. For Ni, valance states consist of  $4s$  and  $3d$  orbitals. We use a kinetic energy cutoff of 400 eV. We perform self-consistent calculations until the total energy converges to within  $1 \times 10^{-4}$  eV. For DFT+U calculations<sup>16</sup>, we use an on-site Coulomb repulsion  $U$  term of 4 eV<sup>27</sup> for Mn  $d$  orbitals only. The value of  $U$  is selected in order to reproduce photoemission spectra measured for a crystal of Mn<sub>12</sub> molecules<sup>28</sup>.

### III. WHOLE STRUCTURE

We consider a structure whose unit cell is shown in Fig. 1(a). In the unit cell, a single Mn<sub>12</sub> molecule is adsorbed on a FM Ni(111) slab of six atomic layers, via two S atoms. This structure is referred to as ‘whole structure.’ We separately optimize geometries of a bare Ni slab (without a Mn<sub>12</sub> molecule) and an isolated Mn<sub>12</sub> molecule, combining the optimized geometries to construct the whole structure.

Let us discuss the geometry and properties of a bare Ni slab. We find that the equilibrium lattice constant of bulk face-centered-cubic (fcc) Ni equals 3.500 Å (3.522 Å) using SIESTA (VASP), which agrees with experiments<sup>30</sup>. With the lattice constant, a Ni(111) slab of  $1 \times 1 \times 6$  atoms is constructed, and its interlayer separations are optimized with in-plane separations fixed, until the maximum force is less than 0.03 eV/Å for SIESTA (0.02 eV/Å for VASP). The optimized interlayer separations are listed in Table II. The spin moments of the six atomic layers are, from the topmost to the bottommost layers, found to be (0.74, 0.68, 0.64, 0.64, 0.68, 0.74)  $\mu_B$ , respectively, using SIESTA, while they are equal to (0.68, 0.68, 0.65, 0.65, 0.69, 0.68)  $\mu_B$ , respectively, using VASP.

We briefly review the geometry and properties of an isolated  $Mn_{12}$  molecule. More details can be found in Ref.[14]. A standard  $Mn_{12}$  molecule,  $[Mn_{12}O_{12}(CH_3COO)_{16}(H_2O)_4]$ , has the total magnetic moment of 20  $\mu_B$  in the ground state, where the eight outer Mn spins (each  $Mn^{3+}$  having 4  $\mu_B$ ) align antiparallel to the four inner Mn spins (each  $Mn^{4+}$  having 3  $\mu_B$ ). For a standard  $Mn_{12}$  molecule, both the lowest unoccupied molecular orbital (LUMO) and the highest occupied molecular orbital (HOMO) arise from the Mn  $d$  orbitals. To reduce computational cost, we simplify a standard SMM  $Mn_{12}$  into  $[Mn_{12}O_{12}(HCOO)_{16}]$ , where the  $CH_3$  groups in the standard  $Mn_{12}$  are replaced by  $H^{31}$ , and the four water molecules are removed<sup>14</sup>. This simplification does not affect the magnetic core of the  $Mn_{12}$ . We substitute S atoms for the two H atoms closest to the Ni surface [Fig. 1(b)], such that the  $Mn_{12}$  molecule bonds to the Ni surface via the S. The bond length between the C and S equals 1.88 Å (Fig. 1(b), Table I). This slightly modified form of  $Mn_{12}$  is referred to as a S-terminated  $Mn_{12}$ . For a S-terminated  $Mn_{12}$  molecule, the magnetic moments of the Mn ions remain unchanged, but each S atom has the magnetic moment of 1  $\mu_B$  aligned antiparallel to the net magnetic moment of the twelve Mn ions. As a result, a S-terminated  $Mn_{12}$  molecule has the total magnetic moment of 18  $\mu_B$  in the ground state. The magnetic moments listed in Table III are computed by placing a sphere around each atom with the radius given in Table IV. (The radii for O and S used in this work differ from those in Ref.[14].) The atomically resolved magnetic moments (Table III) are lower than the actual values because contributions from inter-atomic regions are not included. For a S-terminated  $Mn_{12}$ , the LUMO and HOMO originate from the S  $p$  orbitals.

We now discuss the geometry of a unit cell of the whole structure. We determine a unit cell in order for the following conditions to be satisfied: (i) one  $Mn_{12}$  molecule must fit the

Ni surface area, (ii) neighboring  $\text{Mn}_{12}$  molecules interact weakly, and (iii) the total number of basis sets per unit cell should be computationally feasible. A monoclinic unit cell of  $17.33 \times 17.33 \times 36.00 \text{ \AA}^3$  ( $17.43 \times 17.43 \times 32.00 \text{ \AA}^3$ ) suffices to meet the above conditions for **SIESTA** (**VASP**). The unit cell [Fig. 1(a)] consists of a  $\text{Mn}_{12}$  molecule attached to a Ni slab of  $7 \times 7 \times 6$  atoms via two S atoms and a vacuum layer of  $13.72 \text{ \AA}$  ( $9.69 \text{ \AA}$ ) for **SIESTA** (**VASP**). The two S atoms bond to hollow sites of the Ni(111) surface and to the C atoms close to the Mn(1), Mn(2), Mn(6), and Mn(10) sites [Figs. 1(b),(c)]. The whole structure contains the total of 382 atoms, equivalent to 3450 valence electrons or 5552 orbitals. We sample  $3 \times 3 \times 1$   $k$ -points for our DFT calculations. Considering the large system size, full geometry relaxations are difficult to achieve. Instead, we carry out partial geometry relaxations using **SIESTA**, where the  $\text{Mn}_{12}$ , S, and Ni surface layer relax with the five Ni layers fixed. We find that the partial geometry relaxations do not alter our findings discussed below. We thus, henceforth, consider the unrelaxed whole structure only. For the unrelaxed geometry, our calculations show that large forces (the  $z$  components only) act mainly on the two S atoms and the six Ni surface atoms bonded to the S. They are, respectively,  $-2.35$ ,  $-2.35$ ,  $1.58$ ,  $1.27$ ,  $1.39$ ,  $1.44$ ,  $1.54$ , and  $1.68 \text{ eV/\AA}$ , using **SIESTA** ( $-1.52$ ,  $-1.52$ ,  $0.93$ ,  $0.70$ ,  $0.69$ ,  $0.73$ ,  $0.74$ , and  $0.86 \text{ eV/\AA}$ , using **VASP**).

## IV. RESULTS AND DISCUSSION

### A. Magnetic coupling type and strength

We consider two spin configurations in the whole structure: (i) a FM configuration where the magnetic moment of the  $\text{Mn}_{12}$  is parallel to the magnetization of the Ni slab, and (ii) an AFM configuration where the magnetic moment of the  $\text{Mn}_{12}$  is now reversed such that it is antiparallel to the magnetization of the Ni slab. Our DFT calculations show that the AFM configuration has a lower energy than the FM one, and that the energy difference between the two configurations equals  $39.5 \text{ meV}$  ( $51.6 \text{ meV}$ ), using **SIESTA** (**VASP**). The exchange-correlation potential within the PBE GGA does not fully treat self-interaction corrections of the localized  $d$  states in the Coulomb potential. As a result, residual self-interactions induce slightly more diffuse  $d$  electrons, which entails overestimated exchange coupling. To examine the effect of self-interaction corrections, we apply a DFT+ $U$  method<sup>16</sup> to the two

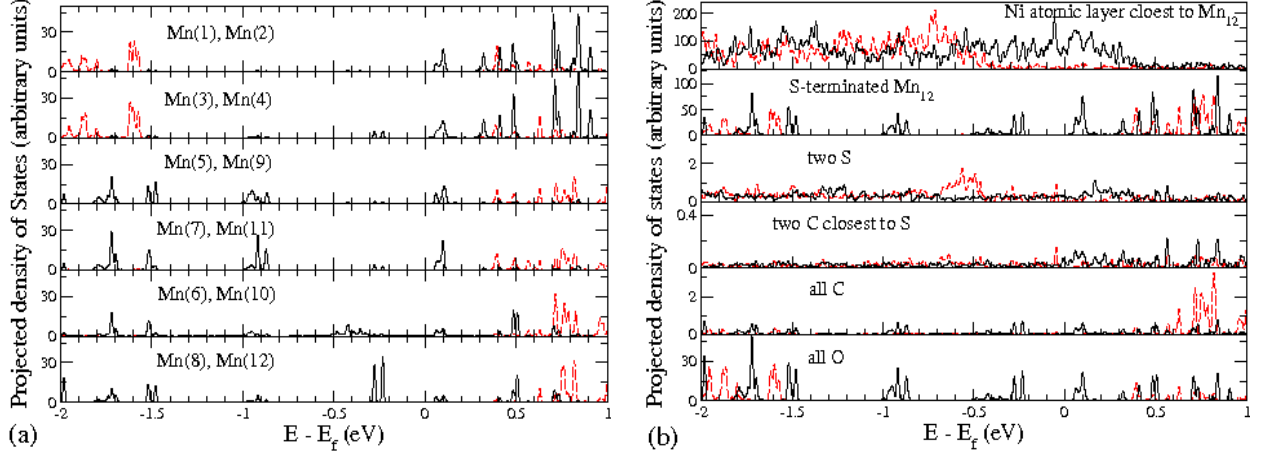


FIG. 2: (Color online) Spin-polarized DOS projected onto (a) the Mn  $d$  orbitals, and (b) the Ni surface  $d$  orbitals, all orbitals of the S-terminated  $\text{Mn}_{12}$ , the  $p$  orbitals of the O, C, and S atoms, and the C  $p$  orbitals bonded to the S atoms. The DOS is calculated for the AFM configuration. The majority (minority) spin is denoted as red dashed (black solid) curves. Notice the different vertical scales in (b).

spin configurations with  $U=4$  eV for the Mn  $d$  orbitals. Our DFT+ $U$  calculations using VASP show that the AFM configuration has still a lower energy than the FM, and that the energy difference equals 46.3 meV. This energy difference does not differ much from that using DFT (Table V), so that we, henceforth, discuss results obtained using DFT, unless specified otherwise.

## B. Electronic properties of the whole structure

We investigate the effect of the Ni slab on the electronic properties of the S-terminated  $\text{Mn}_{12}$  in the AFM configuration. Using a Methfessel-Paxton<sup>32</sup> smearing parameter  $\sigma=0.01$  eV in VASP, we calculate the density of states (DOS) projected onto the Mn  $d$  orbitals, the Ni  $d$  orbitals, and the  $p$  orbitals of the O, S, and C atoms. As shown in Fig. 2(a), the Mn  $d$  orbitals broaden due to interactions with the Ni slab. Large broadening occurs for the  $d$  orbitals of the Mn(6) and Mn(10) sites near 0.5 eV below the Fermi level,  $E_f$ . Notice that the Mn(6) and Mn(10) sites are closest to the Ni surface [Fig. 1(c)]. The O  $p$  orbitals strongly hybridize with the Mn  $d$  orbitals (Fig. 2). In the band structure of Ni [top panel of Fig. 2(b)], the minority-spin  $d$  bands intersect  $E_f$ , while the majority-spin  $d$

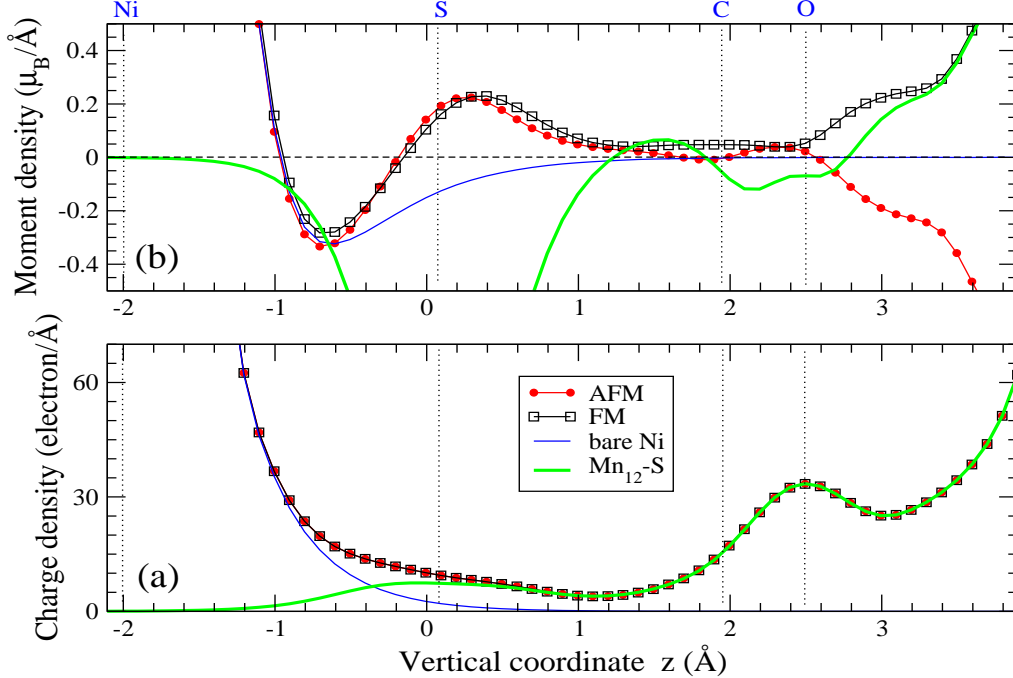


FIG. 3: (Color online) (a) Charge density and (b) magnetic moment density integrated over the  $xy$  plane, as a function of  $z$  for the AFM (red filled circles) and FM (black empty squares) configurations, the bare Ni slab (blue thin solid curve), and the isolated S-terminated  $\text{Mn}_{12}$  (green thick solid curve). The  $z$  coordinates of the Ni surface layer, S, C, and O sites are marked. The Mn sites locate out of the range. The S atoms are located at  $z = 0.09 \text{ \AA}$ , as in Ref.[14].

bands are completely filled. The S  $p$  orbitals and the C  $p$  orbitals bonded to the S atoms are delocalized due to the interactions with the Ni slab [third and fourth panels of Fig. 2(b)]. The S  $p$  orbitals are spin polarized, and strongly hybridize with the surface Ni  $d$  orbitals than the C  $p$  orbitals do.

Let us now discuss the charge distribution of the whole structure as well as calculate charge transfer between the Ni slab and the S-terminated  $\text{Mn}_{12}$  for the FM and AFM configurations. We perform our calculations using VASP. As shown in Fig. 3(a), the charge distribution of the bare Ni slab has a long tail which is deeply penetrated into the region beyond the S. The charge distribution of the whole structure coincides with that of the isolated  $\text{Mn}_{12}$  near the mid-distance between the S and the C [Fig. 3(a)]. To compute the charge transfer, we integrate over the  $xy$  plane the charge density of the whole structure,  $\rho_{\text{whole}}(x, y, z)$ , and the charge density of the isolated S-terminated  $\text{Mn}_{12}$ ,  $\rho_{\text{SMM,isol}}(x, y, z)$ . We then take a difference between the two integrated charge densities:  $\Delta\rho(z) = \int_{xy} (\rho_{\text{whole}} -$



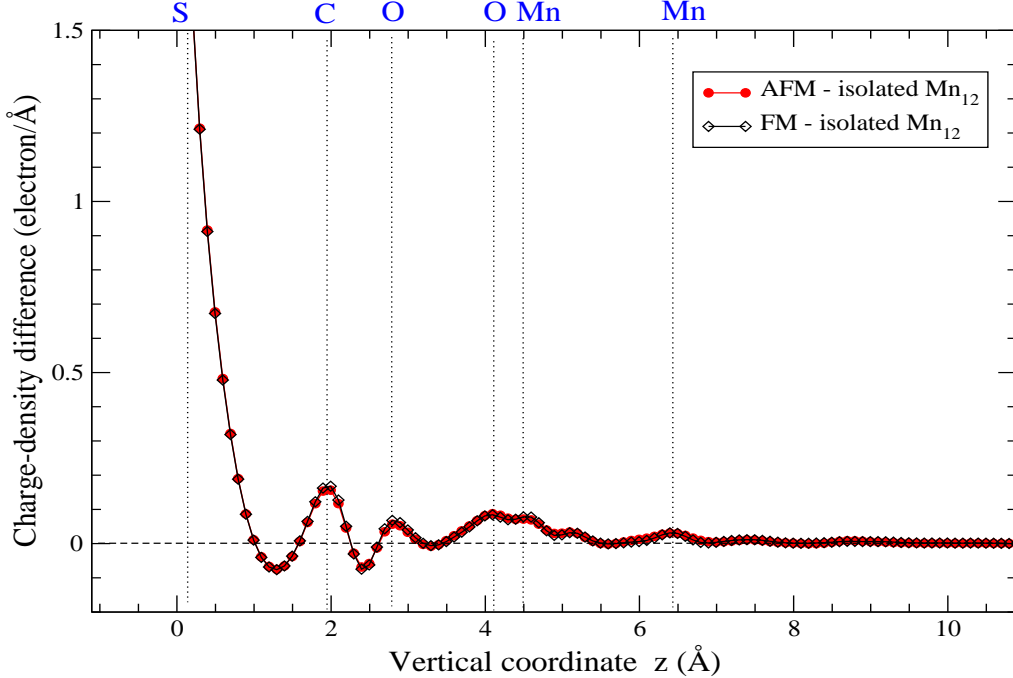


FIG. 4: (Color online) The difference in charge density between the whole structure and the isolated S-terminated  $\text{Mn}_{12}$ ,  $\Delta\rho(z)$ , as a function of  $z$  for the AFM (red filled circles) and FM (black empty diamonds) configurations. The  $z$  coordinates of the S, the C and O closest to the S, and the Mn, are marked.

$\rho_{\text{SMM,isol}})dxdy$ . The charge-density difference,  $\Delta\rho(z)$  (Fig. 4), peaks at the linker molecules, the S, into which the charge distribution of the Ni slab is penetrated [Fig. 3(a)]. We calculate the charge transfer by an integration of  $\Delta\rho(z)$  over  $z$ . We find that some amount of charge is transferred from the Ni slab to the  $\text{Mn}_{12}$  molecule. The magnitude of the charge transfer is sensitive to the lower bound of the integration because the exact boundary between the Ni slab and the  $\text{Mn}_{12}$  is hard to be determined in the whole structure. For instance, when we integrate  $\Delta\rho(z)$  from  $z = -0.94 \text{ \AA}$  to  $z = 11.90 \text{ \AA}$ , the charge transferred equals 13.77 (13.78) electrons for the AFM (FM) configuration. Here  $z = -0.94 \text{ \AA}$  represents the mid-distance between the Ni surface layer and the S, and the S atoms are located at  $z = 0.09 \text{ \AA}$ , as in Ref.[14].

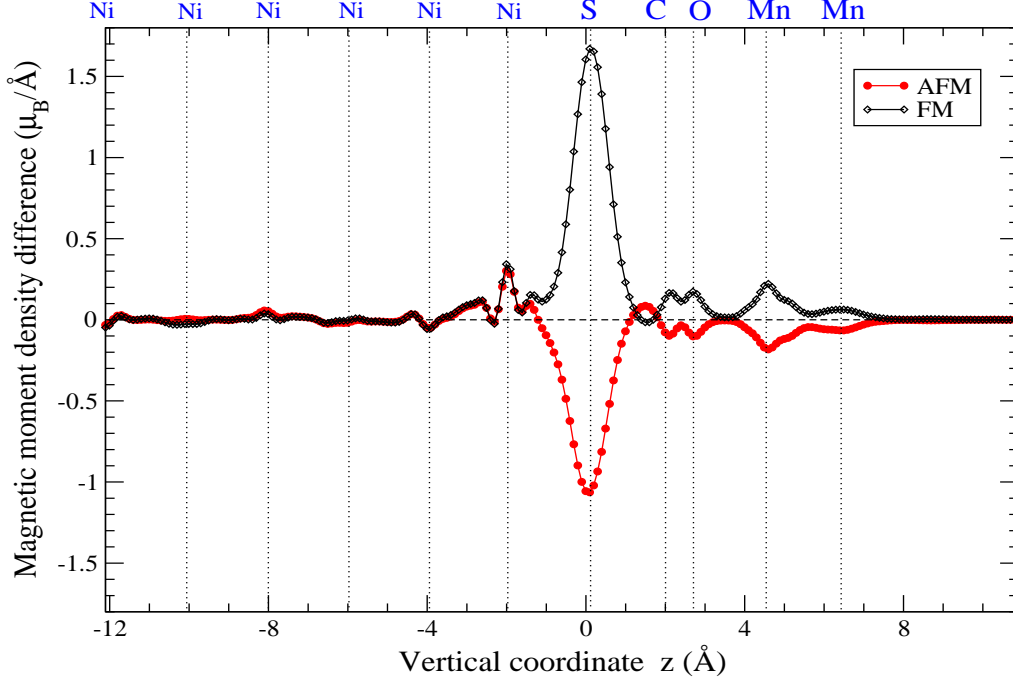


FIG. 5: (Color online) The difference in magnetic-moment density between the whole structure and the sum of the bare Ni slab and the isolated S-terminated  $\text{Mn}_{12}$ ,  $\Delta\rho_M(z)$ , as a function of  $z$  for the AFM (red filled circles) and FM (black empty diamonds) configurations. The  $z$  coordinates of the six Ni atomic layers, the S, the C and O closest to the S, and the Mn, are marked.

### C. Magnetic properties of the whole structure

We examine how the adsorption modifies the magnetic moments of the S-terminated  $\text{Mn}_{12}$  and of the Ni slab as a function of  $z$  for the FM and AFM configurations, using VASP. Similarly to the charge-transfer calculation, we integrate over the  $xy$  plane the spin density of the whole structure,  $\rho_{\text{whole}}^M$ , the spin density of the isolated S-terminated  $\text{Mn}_{12}$ ,  $\rho_{\text{SMM,isol}}^M$ , and the magnetization of the bare Ni slab,  $\rho_{\text{Ni,bare}}^M$ . We refer to these integrated quantities as one-dimensional magnetic-moment densities and magnetization depending on  $z$ . We consider the following difference in one-dimensional magnetic-moment density:  $\Delta\rho_M(z) = \int_{xy} [\rho_{\text{whole}}^M - (\int_{xy} \rho_{\text{Ni,bare}}^M \pm \int_{xy} \rho_{\text{SMM,isol}}^M)] dx dy$ , where the positive (negative) sign in front of the third term is applied to the FM (AFM) configuration. As shown in Fig. 5, the most prominent effects of the adsorption in the difference  $\Delta\rho_M(z)$  are (i) that the difference peaks at the S ions, and (ii) that the AFM configuration possesses a smaller peak amplitude in the difference than the FM configuration does. For the isolated  $\text{Mn}_{12}$ , each S ion has the

magnetic moment of  $1 \mu_B$ , while for the whole structure, the S ions lose the spin polarization to great extent. As a result, the peak in  $\Delta\rho_M(z)$  occurs at the S ions. Notice that in the isolated  $\text{Mn}_{12}$ , the magnetic moment of each S ion aligns antiparallel to the net magnetic moment of the twelve Mn ions [Fig. 3(b)]. In the whole structure, however, the magnetic moment of each S ion aligns parallel to the magnetization of the Ni slab, independent of the sign of the magnetic coupling between the  $\text{Mn}_{12}$  and the Ni slab (Table III). This entails that the peak amplitude for the AFM configuration is smaller than that for the FM configuration. (Effects (i) and (ii) are further discussed in Sec.IV.D.) For the Ni slab, the magnetic moments of the top two layers in proximity to the  $\text{Mn}_{12}$  substantially change due to the interactions with the  $\text{Mn}_{12}$ . As shown in Fig. 6, great changes appear near the sites where the S ions are bonded. The spatial dependence of the magnetic moments induced in the Ni slab for the FM configuration is similar to that for the AFM illustrated in Fig. 6. The main features discussed in this section remain unchanged with the application of the GGA+U method.

Let us now discuss a way to calculate the total magnetic moment induced in the Ni slab,  $\Delta M_{\text{Ni}}^{\text{ind}}$ , and the magnetic moment of the adsorbed  $\text{Mn}_{12}$ ,  $M_{\text{SMM}}^{\text{ads}}$ , within the GGA and GGA+U formalisms, using VASP. The difference in magnetic moment between the whole structure and the bare Ni slab,  $[M_{\text{whole}} - M_{\text{Ni}}^{\text{bare}}]$ , has contributions from both  $\Delta M_{\text{Ni}}^{\text{ind}}$  and  $M_{\text{SMM}}^{\text{ads}}$ , so that  $[M_{\text{whole}} - M_{\text{Ni}}^{\text{bare}}] = M_{\text{SMM}}^{\text{ads}} + \Delta M_{\text{Ni}}^{\text{ind}}$ . We first compute  $[M_{\text{whole}} - M_{\text{Ni}}^{\text{bare}}]$  including contributions from inter-atomic regions. To find the value of  $\Delta M_{\text{Ni}}^{\text{ind}}$ , we integrate the difference in one-dimensional magnetic-moment *density* between the whole structure and the bare Ni slab,  $\int_{xy} (\rho_{\text{whole}}^M - \rho_{\text{Ni,bare}}^M) dx dy$  (Fig. 7), from the  $z$  coordinate of the bottommost Ni layer (farthest from the surface layer,  $z = -12.10 \text{ \AA}$ ) to the mid-distance between the Ni surface layer and the S atoms ( $z = -0.94 \text{ \AA}$ ). Similarly to the charge-transfer calculation, the value of  $\Delta M_{\text{Ni}}^{\text{ind}}$  depends on the upper bound in the integration, and the difference in  $\Delta M_{\text{Ni}}^{\text{ind}}$  between the AFM and FM configurations is very small (Fig. 7). Then using the calculated values of  $[M_{\text{whole}} - M_{\text{Ni}}^{\text{bare}}]$  and  $\Delta M_{\text{Ni}}^{\text{ind}}$ , we find the value of  $M_{\text{SMM}}^{\text{ads}}$ .

Within the GGA, the difference,  $[M_{\text{whole}} - M_{\text{Ni}}^{\text{bare}}]$ , amounts to  $-19.29$  ( $20.54$ )  $\mu_B$  for the AFM (FM) configuration. When we integrate the one-dimensional density difference from  $z = -12.10$  to  $z = -0.94 \text{ \AA}$ , we find that  $\Delta M_{\text{Ni}}^{\text{ind}}$  amounts to  $0.24 \mu_B$  ( $0.23 \mu_B$ ) for the AFM (FM) configuration (Fig. 7). Thus,  $M_{\text{SMM}}^{\text{ads}}$  equals  $-19.53$  ( $20.31$ )  $\mu_B$  for the AFM (FM) configuration. Within the GGA+U formalism, the difference,  $[M_{\text{whole}} - M_{\text{Ni}}^{\text{bare}}]$  reaches

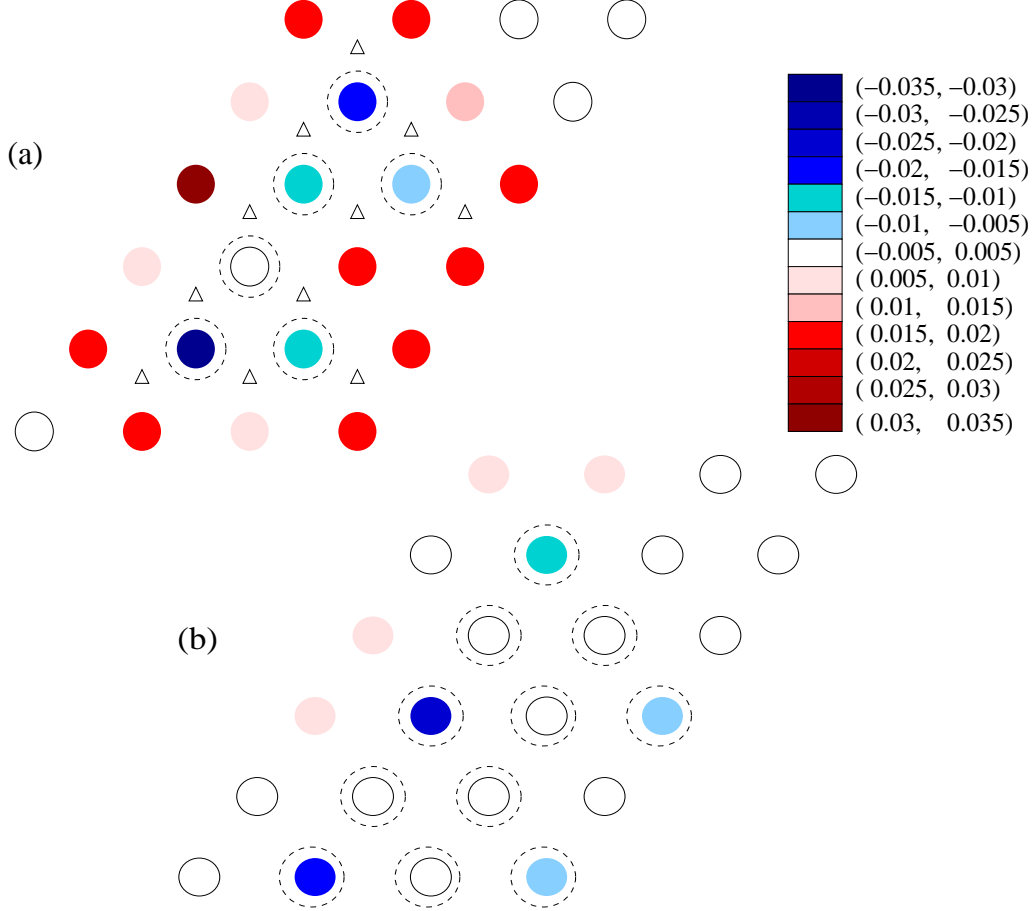


FIG. 6: (Color online) Magnetic moments induced in (a) the topmost Ni surface layer and (b) the second Ni layer from the surface in units of  $\mu_B$  for the AFM configuration. Not all of the Ni sites per atomic layer are shown. The dashed circles in (a) represent the sites where the S ions are bonded. The sites marked by the triangles in (a) correspond to the dashed circles in (b) in the  $xy$  plane.

$-19.05$  ( $20.46$ )  $\mu_B$  for the AFM (FM) configuration. Since the  $U$  term is added to the Mn  $d$  orbitals only, the total magnetic moment induced in the Ni slab would not change with the addition of the  $U$  term. Thus,  $M_{\text{SMM}}^{\text{ads}}$  equals  $-19.29$  ( $20.23$ )  $\mu_B$  for the AFM (FM) configuration. Considering that the magnetic moment of an isolated S-terminated  $\text{Mn}_{12}$  equals  $18 \mu_B$ , induced magnetic moments on the adsorbed  $\text{Mn}_{12}$  are shown in Table VI.

To summarize the above calculations, when a S-terminated  $\text{Mn}_{12}$  molecule is adsorbed on a FM metal such as Ni, both the GGA and GGA+ $U$  calculations suggest that the adsorbed  $\text{Mn}_{12}$  molecule has the magnetic moment deviated from  $20 \mu_B$ , and that the sign of its deviation from  $20 \mu_B$  depends on the sign of the magnetic coupling between the  $\text{Mn}_{12}$  and

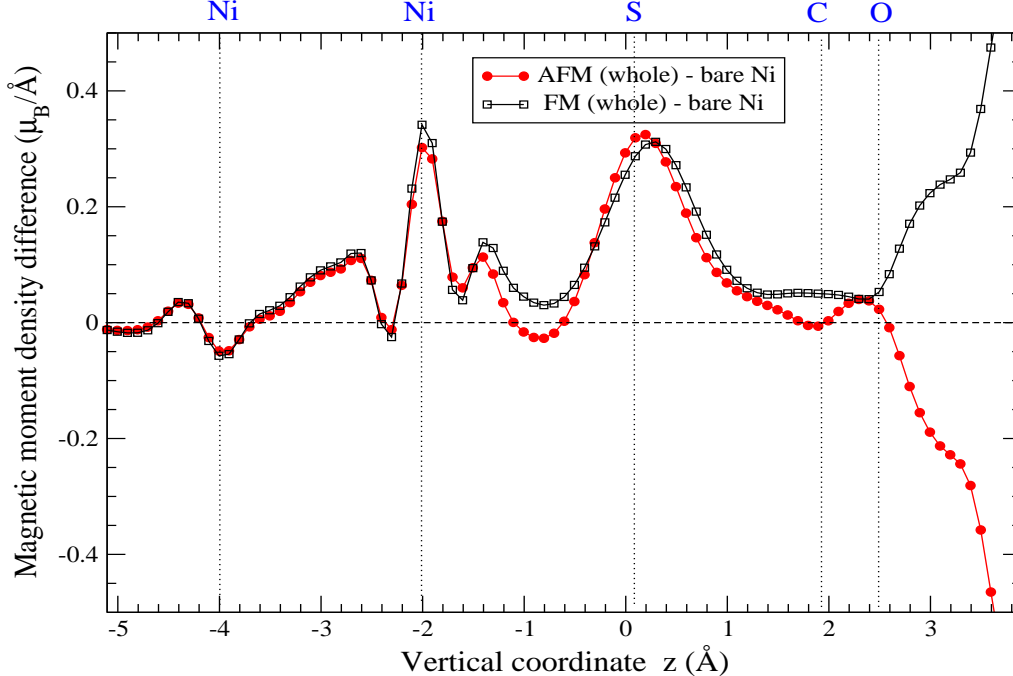


FIG. 7: (Color online) The difference in one-dimensional magnetic-moment density between the whole structure and the bare Ni slab,  $\int_{xy}(\rho_{\text{whole}}^M - \rho_{\text{Ni,bare}}^M)dx dy$ , as a function of  $z$  for the AFM (red filled circles) and FM (black empty squares) configurations.

the FM substrate (Table VI). This result differs from the case that a S-terminated  $\text{Mn}_{12}$  molecule is adsorbed on a non-magnetic metal such as Au. The magnetic moment of a S-terminated  $\text{Mn}_{12}$  adsorbed on Au increases to  $19.8 \mu_B^{14}$ . Notice that an isolated standard  $\text{Mn}_{12}$  molecule has the magnetic moment of  $20 \mu_B$ .

We now investigate the effect of the adsorption on the magnetic anisotropy of the AFM configuration. We perform DFT calculations including SOC using VASP. Considering the large system size, we treat the SOC non-self-consistently in collinear cases. Previous theoretical calculations<sup>14</sup> have shown that a non-self-consistent treatment of SOC produces a slightly lower magnetic anisotropy barrier (lower by 14% for an isolated standard  $\text{Mn}_{12}$ ) than an experimental value or a self-consistently calculated value with a correct magnetic easy axis<sup>14</sup>. Our calculation reveals that a bare Ni(111) slab of six atomic layers possesses the magnetic easy axis parallel to the surface (which agrees with experiments<sup>33</sup>), and that the magnetic anisotropy barrier of the slab ( $7 \times 7 \times 6$  atoms) equals 66.9 meV. An isolated S-terminated  $\text{Mn}_{12}$  molecule has, however, the magnetic easy axis normal to the surface, and its magnetic anisotropy barrier is found to be 4.88 meV. For the whole structure, we consider

only two collinear spin configurations: (i) both the magnetic moment of the  $\text{Mn}_{12}$  and the magnetization of the Ni slab are parallel to the Ni surface, and (ii) they are perpendicular to the surface. Our calculations show that the first collinear configuration provides a lower energy than the second configuration, which implies that the Ni slab prevalently contributes to the magnetic anisotropy of the whole structure. The energy difference between the two collinear configurations equals 55.3 meV. This energy difference is lower than the magnetic anisotropy barrier of the bare Ni slab because for the given molecular orientation the magnetic easy axis of the isolated S-terminated  $\text{Mn}_{12}$  is perpendicular to that of the bare Ni slab. A more quantitative analysis requires a self-consistent treatment of SOC and inclusion of noncollinear spin configurations and dipolar interactions, which is beyond the scope of the current study.

#### D. Mechanisms of magnetic coupling

To understand the mechanisms of the magnetic coupling between the  $\text{Mn}_{12}$  and the Ni slab, we consider direct exchange coupling and superexchange coupling<sup>18</sup>. In the whole structure, the shortest separation between the Mn ions and the Ni surface atoms (6.58 Å) is too large for direct exchange coupling to be effective. Thus, the Ni  $d$  orbitals do not hybridize with the Mn  $d$  orbitals. As a result, superexchange and/or Ruderman-Kittel-Kasuya-Yosida (RKKY)-like interactions<sup>34,35</sup> may cause the magnetic coupling. In numerous systems, either superexchange or RKKY-like interactions play a role in magnetic coupling. In this work, we consider superexchange coupling exclusively because it explains the magnetic coupling of interest.

Let us examine contributions of superexchange interactions to the magnetic coupling. In the whole structure, the shortest separation between the S sites and the Ni surface atoms is set to be 2.52 Å [Fig. 1(b), Table I]. As discussed, charge transfer occurs from the Ni slab to the S-terminated  $\text{Mn}_{12}$  molecule, or to the S ions which is the closest to the Ni slab [Fig. 8(a)]. The fact that the LUMO and HOMO of the  $\text{Mn}_{12}$  arise from the S  $p$  orbitals, corroborates the charge transfer to the S ions. The band structure of Ni entails favorable transfer of minority-spin electrons. Thus, the total magnetic moment induced in the Ni slab,  $\Delta M_{\text{Ni}}^{\text{ind}}$ , is positive (Sec.IV.C), and the difference in one-dimensional magnetic moment density between the whole structure and the bare Ni slab (Fig. 7) has a positive

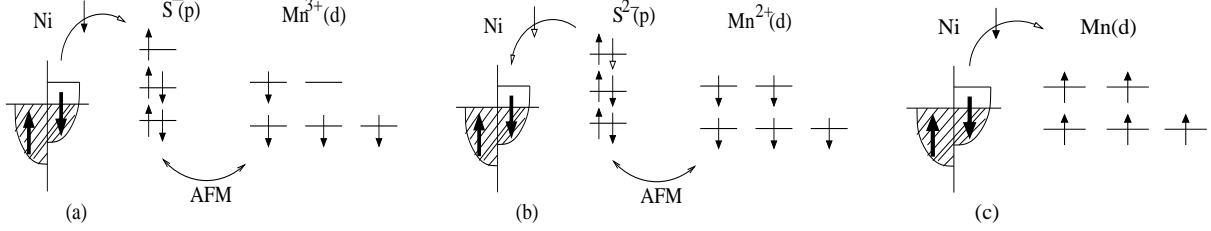


FIG. 8: Magnetic coupling via superexchange interactions for (a) the whole structure and (b) a single Mn atom adsorbed on Ni(111) via S. Magnetic coupling via hybridization for (c) a single Mn atom directly bonded to Ni(111). The majority and minority-spin Ni 3d bands at zero temperature, S 2p orbital levels (degenerate), and Mn 3d orbital levels, are illustrated. The Mn d levels for (b) and (c) are degenerate.

peak amplitude at the Ni surface layer. This charge transfer lowers the magnetic moments of the S ions, resulting in the magnetic moments parallel to the magnetization of the Ni slab [Fig. 8(a)]. Let us now focus on the region between the S and the Mn ions [Fig. 1(b)]. The magnetic moments of the C and O ions closest to the S ions are much smaller than those of the S ions (Table III). As shown in Fig. 1(b), C and O anions are located between the S and the Mn(1) and Mn(6). The bond angle created by the Mn(6) [or Mn(1)] and the O and C bonded to the Mn [Fig. 1(b)] equals 123 degrees. The bond angle of S-C-O in Fig. 1(b) falls on 114-118 degrees. While the S ions have dominant contributions from  $2p_x$  and  $2p_y$  orbitals, the C and O anions have equal contributions from  $2p_x$ ,  $2p_y$ , and  $2p_z$  orbitals. The Mn(1) ( $\text{Mn}^{4+}$ ) possesses exactly half-filled spin-polarized  $t_{2g}$  orbitals. Our calculations suggest that this inner Mn ion is ferromagnetically coupled to the magnetic moments of the S, C, and O ions. The Mn(6) ( $\text{Mn}^{3+}$ ) has spin-polarized half-filled  $t_{2g}$ -like orbitals and quarter-filled  $e_g$ -like orbitals. Our calculations indicate that the outer Mn ion is antiferromagnetically coupled to the magnetic moments of the S, C, and O ions. The same logic is applied to the other linker molecule. Therefore, the magnetic moments of the S, C, and O ions are antiferromagnetically coupled with the net magnetic moment of the twelve Mn ions. As a result, the superexchange interactions render overall AFM coupling between the local magnetic moments of the Ni and the total magnetic moment of the Mn ions via the S, C, and O p orbitals [Fig. 8(a)]. We emphasize that not only the separation between the Ni and the Mn ions but also the type and geometry of bonding to the Ni and Mn, play an important role for the superexchange interactions.

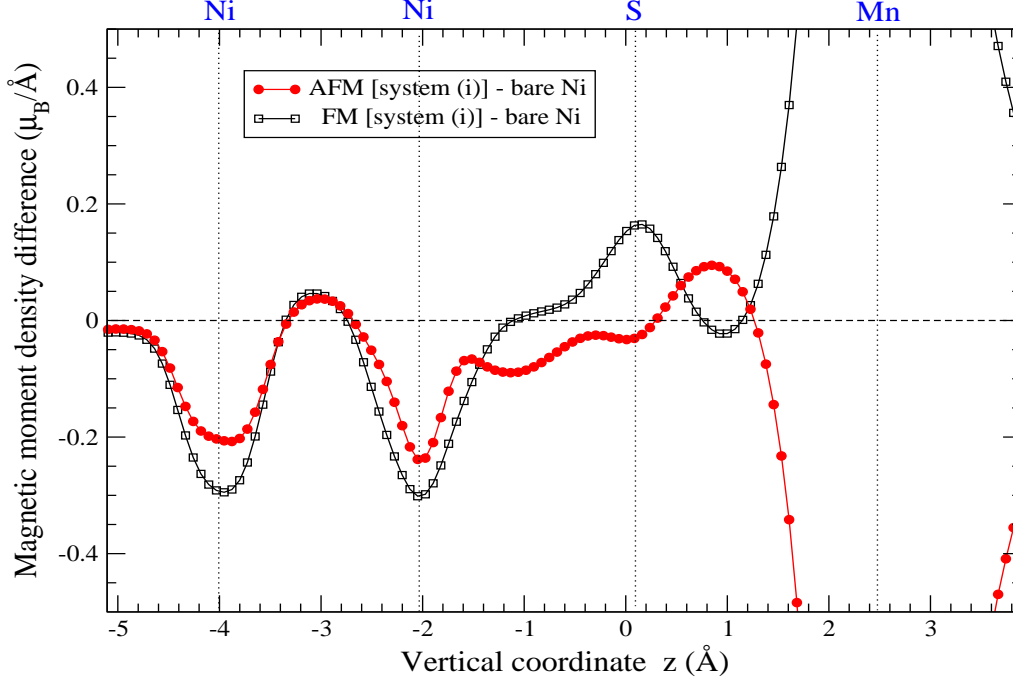


FIG. 9: (Color online) The difference in one-dimensional magnetic-moment density between system (i) and the bare Ni slab,  $\int_{xy} (\rho_{\text{system (i)}}^M - \rho_{\text{Ni,bare}}^M) dx dy$ , as a function of  $z$  for the AFM (red filled circles) and FM (black empty squares) configurations. Calculated using VASP.

To gain further insight into the nature of the magnetic coupling, we investigate magnetic coupling in the following testbed systems: (i) a single Mn atom adsorbed on a Ni(111) slab via one S atom [Fig. 8(b)], and (ii) one Mn atom directly bonded to a Ni(111) slab [Fig. 8(c)]. The magnetic coupling in system (i) seems to have similar mechanisms to that in the whole structure, in that the magnetic moment of the Mn interacts with the Ni slab through the S, and yet system (i) is much simpler than the whole structure. Now if we remove the S atom from system (i) and bring the Mn atom closer to the Ni slab, the characteristics of the magnetic coupling are qualitatively modified. That is the case for system (ii).

Let us first discuss the magnetic coupling in system (i). We set the shortest distance between the S and Ni surface atoms to be the same as that for the whole structure (Table I), and assign positive spin polarization to the Ni slab in both AFM and FM configurations. The S ion bonds to hollow sites of a Ni slab of  $5 \times 5 \times 6$  atoms, and the bond angle of Mn-S-Ni equals  $145.5^\circ$ . Our DFT calculations using SIESTA suggest that similarly to the whole structure, the Mn ion favors AFM coupling to the Ni slab via the S anion (Table I). As in the whole structure, a major contribution to the magnetic coupling originates from



a superexchange interaction via the S anion. An isolated Mn-S dimer has the ground-state spin of  $S = 5/2$ , where the Mn ion carries most of the spin polarization. Since the S  $p$  orbitals are completely filled and the minority-spin Ni  $d$  bands are not fully filled, minority-spin electrons can be transferred now from the S to the Ni slab [Fig. 8(b)]. Consequently, the S  $p$  orbitals possess slight spin polarization parallel to the magnetization of the Ni slab, and negative magnetic moments are induced in the Ni slab (Fig. 9). The S  $p$  orbitals are antiferromagnetically coupled to the Mn  $d$  orbitals. Overall, this leads to AFM coupling between the Mn and the Ni (Fig. 8(b), Table I). The magnetic coupling in system (i) is stronger than that in the whole structure due to the following reasons: (1) The vertical separation between the Mn and the Ni surface atoms in system (i) is shorter than that in the whole structure (Table I). (2) A superexchange interaction through S is stronger than that via O or C, since S atoms more diffuse. In the whole structure, the superexchange interactions are weakened by pathways through the S, C, and O orbitals. For the given geometry of system (i), whether the  $3d$  orbital levels of the adatom are less than or more than half-filled, would not change the sign of the magnetic coupling because the magnetic coupling is mainly governed by a superexchange interaction.

We now examine the magnetic coupling in system (ii). In this system, the Mn atom directly bonds to hollow sites of a Ni slab of  $5 \times 5 \times 6$  atoms, and the Mn  $d$  orbital levels are exactly half-filled [Fig. 8(c)]. Our DFT calculations using **SIESTA** show that stable FM coupling is formed between the Mn and the Ni (Table I), in contrast to system (i) and the whole structure. In system (ii), the bond length between the Mn and the Ni is short (Table I), and so the minority-spin Mn  $d$  orbitals hybridize with the minority-spin Ni  $d$  orbitals. This results in FM coupling between the Mn and the Ni, which agrees with other theoretical calculations<sup>36</sup>. In system (ii), if the  $3d$  orbital levels of the adatom are less than half-filled, then hybridization favors AFM coupling between the adatom and the Ni<sup>36</sup>.

## V. CONCLUSION

We have investigated magnetic coupling between the SMM Mn<sub>12</sub> and a FM Ni(111) substrate, using DFT and a DFT+U method. Our DFT and DFT+U calculations have shown that the Mn<sub>12</sub> interacts antiferromagnetically with the Ni substrate via S, and that the magnetic moment of the Mn<sub>12</sub> is deviated from that of an isolated standard Mn<sub>12</sub>, due to

interactions with the Ni substrate. We have also found that the magnetic anisotropy of the whole structure is dictated by the anisotropy of the Ni slab, and that the magnetic anisotropy barrier of the whole structure depends on the orientation of the Mn<sub>12</sub> relative to the Ni slab. The magnetic coupling is mainly caused by superexchange interactions between the magnetic moments of the Ni and Mn via the S, C, and O anions. Superexchange interactions take into account the bonding types and bonding geometries of linker molecules to the Ni slab and the Mn<sub>12</sub>. Our findings can be observed in XMCD experiments and provide insight into magnetic coupling of other types of SMM to FM substrates.

### Acknowledgments

K.P. was supported by NSF DMR-0804665 and the Jeffress Memorial Trust Funds. The author thanks Salvador Barraza-Lopez and Jaime Ferrer for discussions and reading the manuscript, and thanks Jean J. Heremans for discussions. Computational support was provided by the SGI Altix Linux Supercluster (Cobalt) and Intel 64 Cluster (Abe) at the National Center for Supercomputing Applications under DMR060011, and by Virginia Tech Linux clusters and Advanced Research Computing.

- 
- <sup>1</sup> J. R. Friedman, M. P. Sarachik, J. Tejada, and R. Ziolo, Phys. Rev. Lett. **76**, 3830 (1996).
  - <sup>2</sup> E. M. Chudnovsky and J. Tejada, *Macroscopic Quantum Tunneling of the Magnetic Moment*, Cambridge Studies in Magnetism Vol. 4 (Cambridge University Press, Cambridge, 1998).
  - <sup>3</sup> A. Cornia, A. C. Fabretti, M. Pacchioni, L. Zoppi, D. Bonacchi, A. Caneschi, D. Gatteschi, R. Biagi, U. Del Pennino, V. De Renzi, L. Gurevich, and H. S. J. van der Zant, Angew. Chem. Int. Ed. **42**, 1645 (2003).
  - <sup>4</sup> B. Fleury, L. Catala, V. Huc, C. David, W.Z. Zhong, P. Jegou, L. Baraton, S. Palacin, P.A. Albouy, and T. Mallah, Chem. Comm. **15**, 2020 (2005).
  - <sup>5</sup> Z. Salman, K.H. Chow, R.I. Miller, A. Morello, T.J. Parolin, M.D. Hossain, T.A. Keeler, C.D.P. Levy, W.A. MacFarlane, G.D. Morris, H. Saadaoui, D. Wang, R. Sessoli, G.G. Condorelli, and R.F. Kiefl, Nano. Lett. **7**, 1551 (2007).
  - <sup>6</sup> S. Voss, M. Fonin, U. Rudiger, M. Burgert, U. Groth, and Y.S. Dedkov, Phys. Rev. B **75**,

- 045102 (2007).
- <sup>7</sup> S. Voss, O. Zander, M. Fonin, U. Rudiger, M. Burgert, and U. Groth, Phys. Rev. B **78**, 155403 (2008).
  - <sup>8</sup> M. Mannini, F. Pineider, P. Sainctavit, C. C. D. Moulin, M. A. Arrio, A. Cornia, D. Gatteschi, and R. Sessoli, Eur. Phys. J. Special Topics **169**, 167 (2009).
  - <sup>9</sup> U. del Pennino, V. Corradini, R. Biagi, V. De Renzi, F. Moro, D. W. Boukhvalov, G. Panaccione, M. Hochstrasser, C. Carbone, C. J. Milios, and E. K. Brechin, Phys. Rev. B **77**, 085419 (2008).
  - <sup>10</sup> M. Mannini, F. Pineider, P. Sainctavit, C. Danieli, E. Otero, C. Sciancalepore, A. M. Talarico, M. A. Arrio, A. Cornia, D. Gatteschi, and R. Sessoli, Nature Materials **8** 194, (2009).
  - <sup>11</sup> V. Corradini, F. Moro, R. Biagi, V. De Renzi, U. del Pennino, V. Bellini, S. Carretta, P. Santini, V. A. Milway, G. Timco, R. E. P. Winpenny, and M. Affronte, Phys. Rev. B **79**, 144419 (2009).
  - <sup>12</sup> L. Vitali, S. Fabris, A. M. Conte, S. Brink, M. Ruben, S. Baroni, and K. Kern, Nano Lett. **8**, 3364 (2008).
  - <sup>13</sup> E. Coronado, S. Cardona-Serra, J. M. Clemente-Juan, C. Marti-Castaldo, and E. Navarro-Morafalla, talk at the 6th International Workshop on Nanomagnetism and Superconductivity, Coma-Ruga, Spain (2010).
  - <sup>14</sup> S. Barraza-Lopez, M. C. Avery, and K. Park, Phys. Rev. B **76**, 224413 (2007).
  - <sup>15</sup> J. Nogués, J. Sort, V. Langlais, V. Skumryev, S. Surináčh, J. S. Muñoz, and M. D. Baró, Phys. Rep. **422**, 65 (2005).
  - <sup>16</sup> V. I. Anisimov, F. Aryastawan, and A. I. Lichtenstein, J. Phys.: Condens. Matter **9**, 767 (1997).
  - <sup>17</sup> S. L. Dudarev, G. A. Botton, S. Y. Savrasov, C. J. Humphreys, and A. P. Sutton, Phys. Rev. B **57**, 1505 (1998).
  - <sup>18</sup> J. B. Goodenough, *Magnetism and the Chemical Bond* (John Wiley & Sons, Inc., New York, 1963).
  - <sup>19</sup> J. M. Soler, E. Artacho, J. D. Gale, A. García, J. Junquera, P. Ordejón, and D. Sánchez-Portal, J. Phys.: Condens. Matter **14**, 2745 (2002); J. Junquera, Ó. Paz, D. Sánchez-Portal and E. Artacho, Phys. Rev. B **64**, 235111 (2001); P. Ordejón, D. A. Drabold, M. P. Grumbach and R. M. Martin, Phys. Rev. B **51**, 1456 (1995).
  - <sup>20</sup> G. Kresse and J. Furthmüller, Phys. Rev. B **54**, 11169 (1996); G. Kresse and J. Furthmüller, Phys. Rev. B **59**, 1758 (1999).
  - <sup>21</sup> J. P. Perdew, K. Burke, and M. Ernzerhof, Phys. Rev. Lett. **77**, 3865 (1996).

- <sup>22</sup> N. Troullier and J. L. Martins, Phys. Rev. B **43**, 1993 (1991).
- <sup>23</sup> For construction of pseudopotentials, matching radii provided by the ABINIT team in the official SIESTA website were used.
- <sup>24</sup> J. Junquera, O. Paz, D. Sánchez-Portal, and E. Artacho, Phys. Rev. B **64**, 235111 (2001).
- <sup>25</sup> S. Barraza-Lopez, K. Park, V. García-Suárez, and J. Ferrer, Phys. Rev. Lett. **102**, 246801 (2009).
- <sup>26</sup> P. E. Blöchl, Phys. Rev. B **50**, 17953 (1994).
- <sup>27</sup> S. Barraza-Lopez, M. C. Avery, and K. Park, J. Appl. Phys. **103**, 07B907 (2008).
- <sup>28</sup> U. Del Pennino, V. D. Renzi, R. Biaggi, V. Corraldini, L. Zobbi, A. Cornia, D. Gatteschi, F. Bondino, E. Magnano, M. Zangrando, M. Zacchigna, A. Lichtenstein, and D. W. Boukhvalov, Surf. Sci. **600**, 4185 (2006).
- <sup>29</sup> K. Park, S. Barraza-Lopez, V. García-Suárez, and J. Ferrer, Phys. Rev. B **81**, 125447 (2010).
- <sup>30</sup> A. Taylor, J. Inst. Metals, **77**, 585 (1950); M.P. Marder, *Condensed Matter Physics* (John Wiley & Sons, Inc., New York, 2000).
- <sup>31</sup> M. R. Pederson and S. N. Khanna, Phys. Rev. B **60**, 9566 (1999).
- <sup>32</sup> M. Methfessel and A. T. Paxton, Phys. Rev. B **40**, 3616 (1989).
- <sup>33</sup> W. L. O'Brien and B.P. Tonner, Phys. Rev. B **49**, 15370 (1994).
- <sup>34</sup> J. M. Ziman, *Principles of the theory of solids*, 2nd edition (Cambridge University Press, Cambridge, 1972).
- <sup>35</sup> A. C. Hewson, *The Kondo Problem to Heavy Fermions* (Cambridge University Press, Cambridge, 1993).
- <sup>36</sup> S. Lounis, Ph. Mavropoulos, P. H. Dederichs, and S. Blügel, Phys. Rev. B **72**, 224437 (2005).

TABLE I: Vertical distances  $z$  (in Å), bond lengths  $d$  (in Å), and an energy difference  $\Delta E$  (in eV) between the AFM and FM configurations.  $\Delta E < 0$  ( $\Delta E > 0$ ) implies stable AFM (FM) coupling. For the calculations of  $\Delta E$  using **SIESTA**, we sample  $3 \times 3 \times 1$   $k$ -points for the whole structure and  $4 \times 4 \times 1$   $k$ -points for systems (i) and (ii).

	$z_1 = z(\text{Ni-S})$	$z_2 = z(\text{S-Mn})$	$d(\text{Ni-Mn})$	$d(\text{Ni-S})$	$d(\text{S-C})$	$\Delta E$
whole structure	2.08	4.48	6.58	2.52	1.88	-0.0395
system (i)	2.08	2.40	4.70	2.52	N/A	-0.1050
system (ii)	N/A	N/A	2.80	N/A	N/A	0.1692

TABLE II: Optimized interlayer separations (in Å) for the Ni slab of six atomic layers.  $\Delta z_{ij}$  indicates the vertical distance between the  $i$ th and the  $j$ th layers.  $a$  is the equilibrium lattice constant for bulk fcc Ni.

	SIESTA	VASP
$\Delta z_{12}$	2.011	2.008
$\Delta z_{23}$	2.028	2.037
$\Delta z_{34}$	2.021	2.039
$\Delta z_{45}$	2.023	2.029
$\Delta z_{56}$	2.011	2.007
$a$	3.500	3.522

TABLE III: Atomically resolved magnetic moments for an isolated S-terminated  $\text{Mn}_{12}$  and the AFM and FM configurations, in units of Bohr magneton ( $\mu_B$ ), within the GGA, using VASP. The numbers in the parentheses denote magnetic-moment differences between the isolated  $\text{Mn}_{12}$  and the whole structure, where only the magnitudes are listed. The Mn ions are labeled in Fig. 1(c). In the last row, the total magnetic moment of the  $\text{Mn}_{12}$  is calculated from the sum of the atomically resolved magnetic moments.

Atomic species	isolated S-terminated $\text{Mn}_{12}$	whole, AFM	whole, FM
Mn(1) or Mn(2)	-2.63	2.62 (0.01)	-2.60 (0.03)
Mn(3) or Mn(4)	-2.59	2.59 (0.00)	-2.58 (0.01)
Mn(5) or Mn(9)	3.53	-3.54 (0.01)	3.54 (0.01)
Mn(7) or Mn(11)	3.52	-3.54 (0.02)	3.54 (0.02)
Mn(6) or Mn(10)	3.50	-3.56 (0.06)	3.57 (0.07)
Mn(8) or Mn(12)	3.56	-3.57 (0.01)	3.57 (0.01)
Mn (total)	17.78	-18.00 (0.22)	18.05 (0.27)
O closest to S	-0.01, -0.01, -0.04, -0.04	0.00, 0.00, 0.00, 0.00	0.01, 0.01, 0.02, 0.02
O (total)	0.33	-0.44	0.53
C closest to S	0.01, 0.01	0.01, 0.01	0.00, 0.00
C (total)	0.21	-0.18	0.19
S(1) or S(2)	-0.44	0.09	0.10
$\text{Mn}_{12}$ (total)	17.44	-18.41	18.95

TABLE IV: The atomic sphere radii used for calculations of atomically resolved magnetic moments using VASP (Table III).

Atomic species	Atomic radius (Å)
Ni	1.29
Mn	1.32
S	1.16
O	0.82
C	0.86
H	0.37

TABLE V: Energy difference  $\Delta E$  (in eV) between the AFM and FM configurations, within DFT and DFT+ $U$  formalisms, using SIESTA and VASP.

GGA, SIESTA	GGA, VASP	GGA+ $U$ , VASP
-0.0395	-0.0516	-0.0463

TABLE VI: Total and induced magnetic moments (in  $\mu_B$ ) of the adsorbed  $Mn_{12}$  for the AFM and FM configurations, within the GGA and GGA+ $U$  formalisms, using VASP. The induced moments are obtained from comparison with the magnetic moment of an isolated S-terminated  $Mn_{12}$ .

	Total (GGA)	Induced (GGA)	Total (GGA+ $U$ )	Induced (GGA+ $U$ )
AFM	-19.53	-1.53	-19.29	-1.29
FM	20.31	2.31	20.23	2.23